

## Using the RSM method of improving process parameters of welding AISI 316 and nickel 201 using CO<sub>2</sub> laser

Krishna Kumar G.<sup>1</sup> , Velmurugan C.<sup>2</sup>, Kannan T.<sup>3</sup>

<sup>1</sup>Nehru Institute of Engineering and Technology, Department of Mechatronics Engineering, Nehru Gardens, Nehru College Road, T.M. Palayam, Coimbatore, Tamilnadu 641105, India.

<sup>2</sup>Kumaraguru College of Technology, Department of Mechanical Engineering, Athipalayam Rd, Chinnavedampatti, Coimbatore, Tamilnadu 641049, India.

<sup>3</sup>SVS College of Engineering, Department of Mechanical Engineering, J.P. Nagar, via-Myleripalayam, Arasampalayam, Coimbatore, Tamilnadu 642109, India.

e-mail: gkknehr@gmail.com, c\_velmurugan16@yahoo.co.in, kannan\_kct@yahoo.com

### ABSTRACT

The dissimilar butt welding of nickel 201 and AISI 316 was studied by utilising a 4 kW CO<sub>2</sub> laser with the help of Response Surface Methodology (RSM). The effects of laser power are 2580–3420 W; welding speed 450–1150 mm/s; focal position –1 to 0 mm; beam angle 84–96 degrees; and beam offset 0–0.2 mm on weld geometry, i.e., depth of penetration, bead width, and the Fusion Zone Area (FZ). The required weld profile responses for dissimilar butt welding were modeled mathematically. The constructed models were tested using the sequential F-test, lack of fit test, and analysis of variance (ANOVA). Mathematical models are reflected in the output answers within the parameters of the input process. This laser welding process with an optimal condition zone was discovered using a numeric optimization technique. It aids in the optimization of this process's regulated responses by allowing for more effective parameter combinations. It is clear from the tensile test results that the expected weld strength has been achieved. There is some delta ferrite found in the interdendritic zone in the microstructure and the solidification process reveals columnar grains.

**Keywords:** Weld Bead Geometry; AISI 316 Stainless Steel; Nickel 201; RSM.

### 1. INTRODUCTION

The CO<sub>2</sub> laser welding technique is widely used in the aerospace, automotive, electronic, and nuclear power industries, among others, because of its accuracy, speed, little heat affected zone, and distortion minimization with high power [1, 2]. The laser beam can be focused to produce a tiny spot with an optical intensity of 106 to 1010 W/cm<sup>2</sup>. As a result, the material can be heated to a precise temperature in a short span of time. It takes nanoseconds for a substance to reach its melting point [3, 4]. Thermal conduction, which saves energy by transferring heat from one metal surface to another, is a major benefit of the keyhole form. Maintaining a safe metal-to-metal distance is essential. The material's surface melting power is extremely low [5]. Nd: YAG laser welding of titanium tubes by adjusting the welding speed. According to this study, the titanium tube's ultimate tensile strength was 342 MPa and it was broken at the base metal [6].

The power of a laser beam is a function of the diameter of the beam. By increasing the laser beam intensity, it is necessary to keep the beam diameter constant in order to improve the tonnage ratio. Penetration is also influenced by the laser speed [7–10]. When joining tough materials like titanium or quartz, laser beam welding eliminates the need for any filler material. A laser beam is a numerically controlled, fully automated, high-speed system [11–12] formalised paraphrase. Because of the advantages of laser beam welding over traditional welding, the results reveal improved complete penetration welding in thicker sheets [13–17]. The material gap of between 0.2 and 0.3 mm is likewise good in terms of mechanical properties for the wider weld width. It was observed that laser welding had a specific advantage for small-scale welds. This is mostly due to the extremely small laser beam diameter, which can be precisely aimed at the desired place [18].

The dissimilar junction between austenitic steel and low carbon steel and its weld bead area and shape. The Taguchi method and experimental design were used to evaluate laser parameters, laser power, welding speed, and focus location [19]. The dissimilar metal joint components were manufactured using traditional joining methods for

a variety of applications. The typical joining procedures and unstable welding process parameters, on the other hand, resulted in coarser grain and deformations [20]. It is critical that the laser power, welding speed, focal location and beam angle, offset distance, and shielding gas be precisely chosen to manage the weld bead geometry and heat input.

RSM is a well-known design of experiments (DoE) type that may be applied in various fields to find various input parameters and output responses by using precise material, time, and effort. The Response surface approach is one of the most effective methods for visualising the influence of input parameters on process output responses [21–26]. A variety of input parameters are taken into consideration while determining the weld bead shape, such as depth of penetration, bead width, and the Fusion Zone Area, for dissimilar butt joints between nickel 201 and AISI 316 using an 8 kilowatt CO<sub>2</sub> laser welding equipment in this study. It was found that when using a RSM, the input process parameters such as laser power and welding speed, as well as the output responses such as depth of penetration, bead width, and Fusion Zone Area (FZ), were all related. However, primarily interested in finding the best possible solution that maximises penetration depth and minimises the diameter of the bead and the Fusion Zone Area (FZ). By adjusting the laser intensity, the dissimilar butt joint with and without nickel coating was used to study AZ31 Mg to Ti-6Al-4V. Thermodynamic formulation was also used to clarify mechanical and microstructural details. The fusion zone and titanium interface of the magnesium base metal and other samples failed [27].

Only a specific combination of materials can be welded together. Very few studies have been published on high-power CO<sub>2</sub> laser beam welding of dissimilar material compositions, particularly in the combination of AISI 316 and nickel 201 by an autogenous approach.

## 2. MATERIALS AND METHODS

### 2.1. Experimental design

A five-level central composite design (CCD) with a half fraction was used for the experimental design. Independent variables include laser power; welding speed of 450–1150 mm/min; focal position of –1 to 0 mm; beam angle of 84–96 degrees; and beam offset towards the nickel side of 0–0.2 mm. Data from RSM experiments is analysed using DoE 11 statistical software. Linear and second order polynomial regression equations were created by fitting these polynomials to the experimental data. The constructed models were tested using the F-test, the lack of fit test, and the ANOVA [28]. The mathematical model in terms was identified using a step-wise regression method to fit experimental data to a second-order polynomial Equation (1). The same programme was used to create the response graph and the statistical plots [29, 30].

$$Y = b_0 + \sum b_i x_i + \sum b_{ii} x_{ii}^2 + \sum b_{ij} x_i x_j \quad (1)$$

### 2.2. Desirability approach

It's easy to use and adaptable to a variety of responses, making it ideal for use in a survey. Between 0 and 1 is the desired or undesired range for the response  $Y_i$ , which is determined by the Equations (2–5). Responses have a weighting  $W_i$  that can be anything between 0.1 and 10 points. An important role is played by all the input data and output results when performing a desirability analysis. There ways to signify the most important values of (+ and +++++). In order to measure celebrity function, the Equation (6) is used, where  $T_i$ -the target value,  $n$ -the number of answers [31].

- For maximization,

$$d_i = \begin{cases} 0 & Y_i \leq \text{LOW}_i \\ \left( \frac{Y_i - \text{LOW}_i}{\text{High}_i - \text{LOW}_i} \right) w_i & \text{LOW}_i < Y_i < \text{High}_i \\ 1 & Y_i \geq \text{High}_i \end{cases} \quad (2)$$

- For minimization,

$$d_i = \begin{cases} 1 & Y_i \leq \text{LOW}_i \\ \left( \frac{\text{High}_i - Y_i}{\text{High}_i - \text{LOW}_i} \right) w_i & \text{LOW}_i < Y_i < \text{High}_i \\ 0 & Y_i \geq \text{High}_i \end{cases} \quad (3)$$

- For target,

$$d_i = \begin{cases} \left( \frac{Y_i - LOW_i}{T_i - LOW_i} \right) W_{1i} & LOW_i < Y_i < T_i \\ \left( \frac{Y_i - High_i}{T_i - High_i} \right) W_{2i}, & T_i < Y_i < High_i \\ 0 & \text{Otherwise} \end{cases} \quad (4)$$

- For within the range,

$$d_i = \begin{cases} 1 & LOW_i < Y_i < High_i \\ 0 & \text{Otherwise} \end{cases} \quad (5)$$

$$D = \left( \prod_{i=1}^n d_i^{r_i} \right)^{\frac{1}{\sum r_i}} \quad (6)$$

### 2.3. Experimental work

The chemical composition of stainless steel AISI 316 was 18.50% Cr, 11.50% Cr, 0.90% Si, 1.70% Mn, and 0.40% Fe with 0.35% Si and 0.35% Mn remaining as nickel was employed as a work material and the size of each plate was 100 × 50 × 5 mm. It was the trial samples and bead on plate runs that established the range of input process parameters. In these tests, the operating range of the process parameter, which is shown in Table 1, was confirmed by a visual check.

Utilizing a six-axis, 4kW CO<sub>2</sub> universal laser machining centre (Figure 1), the butt welding joint was carried out using design matrix randomization in order to eliminate experimental mistakes. For the shielding gas,

**Table 1:** Experiment levels and process variables.

CODE	FACTOR	UNIT	-2	-1	0	+1	+2
BP	Beam Power	Watts	2580	2790	3000	3210	3420
WS	Welding Speed	mm/min	450	625	800	975	1150
FP	Focal position	Mm	-1	-0.75	-0.5	-0.25	0
BA	Beam Angle	Degrees	84	87	90	93	96
BO	Beam Offset	Mm	0	0.05	0.1	0.15	0.2



**Figure 1:** Experimental setup of TRUMPF LASERCELL TLC1005.

**Table 2:** Design matrix with coded parameters for each process step.

EXP. NO.	BEAM POWER (watts)	WELDING SPEED (mm/min)	FOCAL POSITION (mm)	BEAM ANGLE (degrees)	BEAM OFFSET (mm)
1	-1	-1	-1	-1	1
2	1	-1	-1	-1	-1
3	-1	1	-1	-1	-1
4	1	1	-1	-1	1
5	-1	-1	1	-1	-1
6	1	-1	1	-1	1
7	-1	1	1	-1	1
8	1	1	1	-1	-1
9	-1	-1	-1	1	-1
10	1	-1	-1	1	1
11	-1	1	-1	1	1
12	1	1	-1	1	-1
13	-1	-1	1	1	1
14	1	-1	1	1	-1
15	-1	1	1	1	-1
16	1	1	1	1	1
17	-2	0	0	0	0
18	2	0	0	0	0
19	0	-2	0	0	0
20	0	2	0	0	0
21	0	0	-2	0	0
22	0	0	2	0	0
23	0	0	0	-2	0
24	0	0	0	2	0
25	0	0	0	0	-2
26	0	0	0	0	2
27	0	0	0	0	0
28	0	0	0	0	0
29	0	0	0	0	0
30	0	0	0	0	0
31	0	0	0	0	0
32	0	0	0	0	0

argon flowed at 15 l/m. In order to perform a metallographic investigation, the sample was sectioned along the weldment and polished with emery papers varying in grit size from 100 to 1000. A masking technique utilising aquaregia and Marble's reagents was used to create the etchings. With the use of an optical metallurgical microscope, the investigation of models Zeiss, Axio Vert. A1. A stereomicroscope was used to carry out the macro investigation at a magnification of 10 $\times$ . The profile is measured by the weld bead using the Model: dhs Imaging System, Ver. 6.02, Germany, MACSCOPE-Z, and Pixel Fox Camera. Tables 2 and 3 show the design matrix as well as the measured output responses.

### 3. RESULT AND DISCUSSIONS

Table 2 of the design matrix was used for the experiment, and each of the 32 samples was produced as illustrated in Figure 2 by cutting it into 32 cross-sections. Every experiment was done meticulously and was cut into sections and prepared for profiling. With emery papers of 100 grit or lower, the weld cross sections were polished. The portions were then lapped with a diamond paste ranging in size from 1–2 microns. The material is removed from the surface very gently throughout the lapping process, resulting in a very smooth surface. Dissimilar joint

**Table 3:** Experimental reactions and their corresponding values.

EXP. NO.	DEPTH OF PENETRATION (DP) mm	BEAD WIDTH (BW) mm	FUSION ZONE AREA (FZ) sq.mm
1	5	3.79	10.66
2	4.794	2.481	10.279
3	4.318	3.178	6.765
4	4.513	2.438	6.892
5	4.806	4.376	12.998
6	4.98	4.085	10.575
7	4.518	1.663	5.222
8	4.738	3.181	8.947
9	4.651	3.776	11.611
10	4.712	4.069	12.95
11	4.882	2.971	7.269
12	4.663	2.975	6.887
13	4.406	4.244	13.149
14	4.518	4.933	14.156
15	4.376	2.83	7.026
16	4.713	3.126	7.704
17	4.387	3.808	8.158
18	4.695	3.356	8.206
19	4.75	4.796	15.293
20	4.512	2.612	6.659
21	4.879	3.392	10.675
22	4.975	3.775	11.225
23	4.775	3.001	7.445
24	4.639	3.568	9.77
25	4.379	3.619	9.927
26	4.516	3.364	9.455
27	4.762	4.002	9.758
28	4.798	3.569	9.792
29	4.772	3.556	10.827
30	4.562	3.832	10.747
31	4.612	3.946	10.332
32	4.544	3.621	8.689

weld portions require etching as a crucial step in the welding process. The masking technique was used with aquaregia and Marble's chemicals. The bead width and the depth of penetration are the main profile dimensions that determine the strength of the beadwork. All 32 samples have been precisely measured in terms of their width and depth. Table 3 lists the experimentally determined values, i.e., the output responses.

### 3.1. Analysis of variance (ANOVA)

The models were validated using analysis of variance, and the model F-ratio should fall within the confidence interval [32, 33]. The DoE V11 statistical software summary shows that the quadratic model is statistically significant for all of the output responses and is assessed [34]. Tables 4–6 of ANOVA yield the final reduced models for the output responses. All models with an  $R^2$  value greater than 4 should have appropriate adequacy and precision as measured by the  $R^2$  adequacy metric. The main effects of beam power (BP), welding speed (WS), beam angle (BA), beam offset (BO), the second order effect of welding speed ( $S^2$ ), the second order effect of focal position ( $FP^2$ ), beam offset ( $BO^2$ ), and the two-level interaction of BP and FP, WS and BA, FP and BA are significant model terms in the depth penetration model. However, the most closely related model term to depth

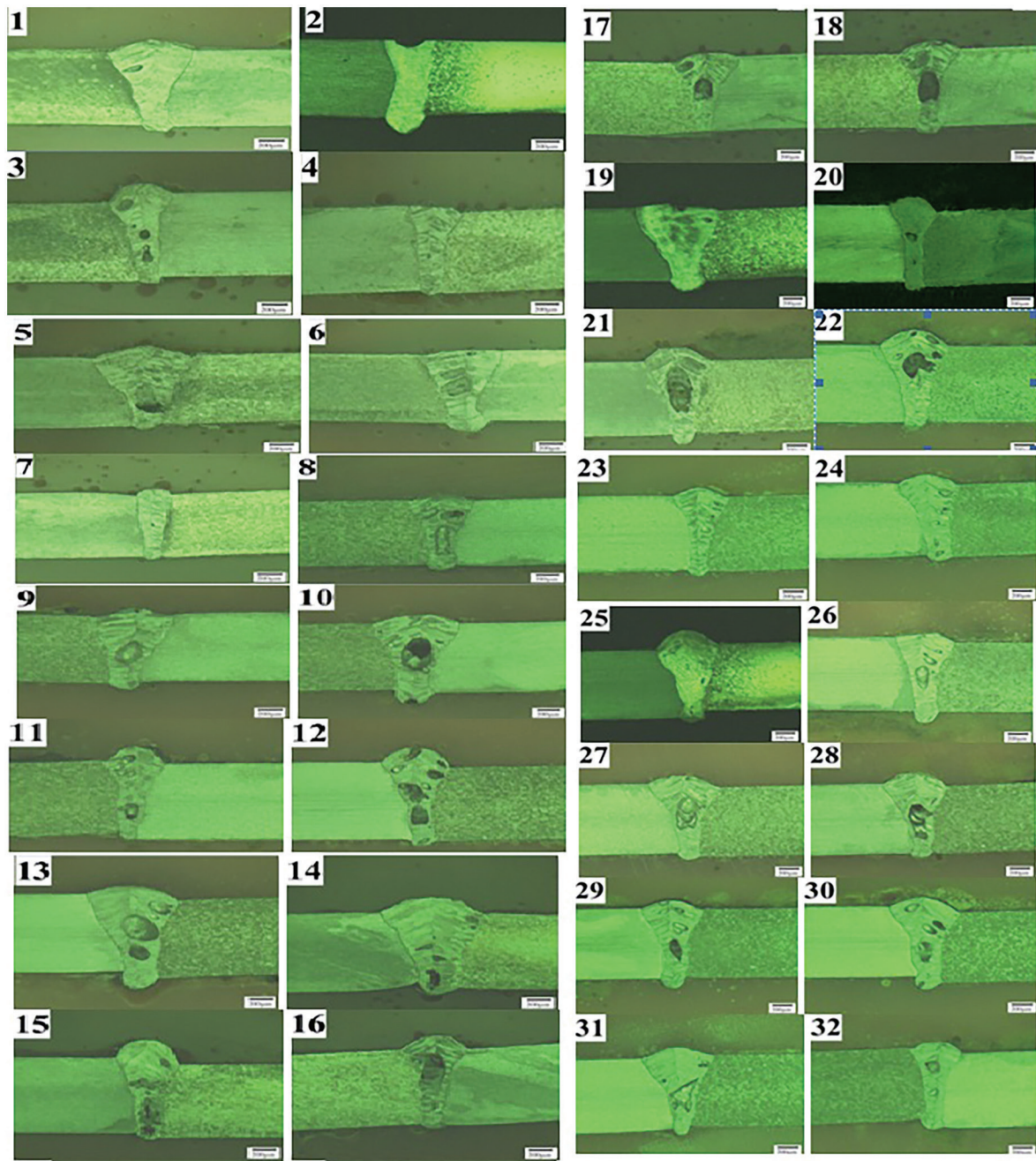


Figure 2: Weld bead of 32 samples after etching at magnification of 10 $\times$ .

penetration is the two-level interaction between WS and BA. The major effects of WS, FP, BA, the second order effects of beam angle (BA<sup>2</sup>), and the two-level interaction of BP and FP, BP and BA, WS and FP, WS and BO, FP and BO are significant model terms for weld bead width. However, the main impact of WS is the most significant model term on the width of the weld bead. W, F, BA, and FP, as well as BP<sup>2</sup>, BA<sup>2</sup>'s two-level interaction with BO, and BO's two-level interaction with BA<sup>2</sup> are significant model terms in the FZ. In this scenario, WS is the most eminent term in the model. In Equations (7), (8), and (9), the last mathematical models are shown in the form of a coded factor (9).

$$\begin{aligned} \text{Depth of Penetration (DP)} = & 4.648 + 0.053 \text{ BP} - 0.067 \text{ WS} - 0.042 \text{ BA} + 0.047 \text{ BO} \\ & + 0.063 \text{ BP FP} + 0.115 \text{ WS BA} - 0.082 \text{ FP BA} + 0.068 \text{ FP}^2 - 0.051 \text{ BO}^2 \end{aligned} \quad (7)$$

$$\begin{aligned} \text{Bead Width (BW)} = & 3.586 - 0.573 \text{ WS} + 0.146 \text{ FP} + 0.202 \text{ BA} + 0.247 \text{ BP FP} \\ & + 0.131 \text{ BP BA} - 0.267 \text{ WS FP} - 0.161 \text{ WS BO} - 0.191 \text{ FP BO} - 0.118 \text{ BA}^2 \end{aligned} \quad (8)$$

**Table 4:** Data from the reduced quadratic model for Depth of Penetration (DP).

SOURCE	SUM OF SQUARES	DF	MEAN SQUARE	F-VALUE	PROB. >F
Model	0.8925	9	0.0992	11.89	<0.0001
BP	0.0693	1	0.0693	8.32	0.0086
WS	0.1096	1	0.1096	13.15	0.0015
BA	0.0432	1	0.0432	5.18	0.0330
BO	0.0536	1	0.0536	6.43	0.0189
BP × FP	0.0640	1	0.0640	7.68	0.0112
WS × BA	0.2116	1	0.2116	25.38	<0.0001
FP × BA	0.1076	1	0.1076	12.90	0.0016
FP <sup>2</sup>	0.1383	1	0.1383	16.59	0.0005
BO <sup>2</sup>	0.0802	1	0.0802	9.62	0.0052
Residual	0.1834	22	0.0083		
Cor. Total	1.08	31			

$R^2 = 0.8295$ ; predicted  $R^2 = 0.6704$ ; adjusted  $R^2 = 0.7598$ ; adequate precision = 15.4620.

**Table 5:** ANOVA table for the BW reduced quadratic model.

SOURCE	SUM OF SQUARES	DF	MEAN SQUARE	F-VALUE	PROB. >F
Model	13.23	9	1.47	22.98	<0.0001
WS	7.89	1	7.89	123.37	<0.0001
FP	0.5180	1	0.5180	8.10	0.0094
BA	0.9866	1	0.9866	15.43	0.0007
BP × FP	0.9821	1	0.9821	15.36	0.0007
BP × BA	0.2767	1	0.2767	4.33	0.0494
WS × FP	1.15	1	1.15	17.94	0.0003
WS × BO	0.4186	1	0.4186	6.55	0.0179
FP × BO	0.5852	1	0.5852	9.15	0.0062
BA <sup>2</sup>	0.4219	1	0.4219	6.60	0.0175
Residual	1.41	22	0.0639		
Cor. Total	14.63	31			

$R^2 = 0.9039$ ; predicted  $R^2 = 0.7426$ ; adjusted  $R^2 = 0.8645$ ; adequate precision = 20.9796.

**Table 6:** ANOVA results for the FZ reduced quadratic model.

SOURCE	SUM OF SQUARES	DF	MEAN SQUARE	F-VALUE	PROB. >F
Model	165.83	8	20.73	38.06	<0.0001
WS	135.06	1	135.06	247.98	<0.0001
FP	2.38	1	2.38	4.38	0.0477
BA	7.11	1	7.11	13.06	0.0015
WS × BA	2.48	1	2.48	4.55	0.0439
FP × BO	4.74	1	4.74	8.70	0.0072
BA × BO	3.09	1	3.09	5.67	0.0259
BP <sup>2</sup>	7.23	1	7.23	13.28	0.0014
BA <sup>2</sup>	4.44	1	4.44	8.16	0.0089
Residual	12.53	23	0.5446		
Cor. Total	178.35	31			

$R^2 = 0.9298$ ; predicted  $R^2 = 0.8726$ ; adjusted  $R^2 = 0.9053$ ; adequate precision = 24.2448.

$$\text{Fusion Zone Area (FZ)} = 10.347 - 2.372 \text{ WS} + 0.315 \text{ FP} + 0.544 \text{ BA} - 0.393 \text{ WS BA} - 0.544 \text{ FP BO} + 0.439 \text{ BA BO} - 0.492 \text{ BP}^2 - 0.385 \text{ BA}^2 \tag{9}$$

The actual factor mathematical model for the responses is given in Equations (10), (11) and (12)

$$\text{Depth of Penetration (DP)} = 20.675 - 0.020 \text{ WS} - 0.211 \text{ BA} + 5.109 \text{ BO} - 0.044 \text{ FP BA} + 1.032 \text{ FP}^2 - 20.821 \text{ BO}^2 \tag{10}$$

$$\text{Bead Width (BW)} = -103.865 - 7.406 \text{ FP} + 2.360 \text{ BA} - 0.012 \text{ WS BO} - 17.050 \text{ FP BO} - 0.013 \text{ BA}^2 \tag{11}$$

$$\text{Fusion Zone Area (FZ)} = -367.12 + 0.053 \text{ WS} + 5.357 \text{ FP} + 7.859 \text{ BA} - 40.967 \text{ FP BO} - 0.273 \text{ BA BO} - 0.039 \text{ BA}^2 \tag{12}$$

### 3.2. Models validation

Figure 3(a), (b), and (c) illustrate the actual and anticipated value associations for DP, BW, and FZ correspondingly. The residual values are in close proximity, which implies that the created models are appropriate. Confirmation experiments are required to check the accuracy of the mathematical models that have been established. Table 7 shows how many of the responses that were analysed were wrongly calculated compared to what their real values were.

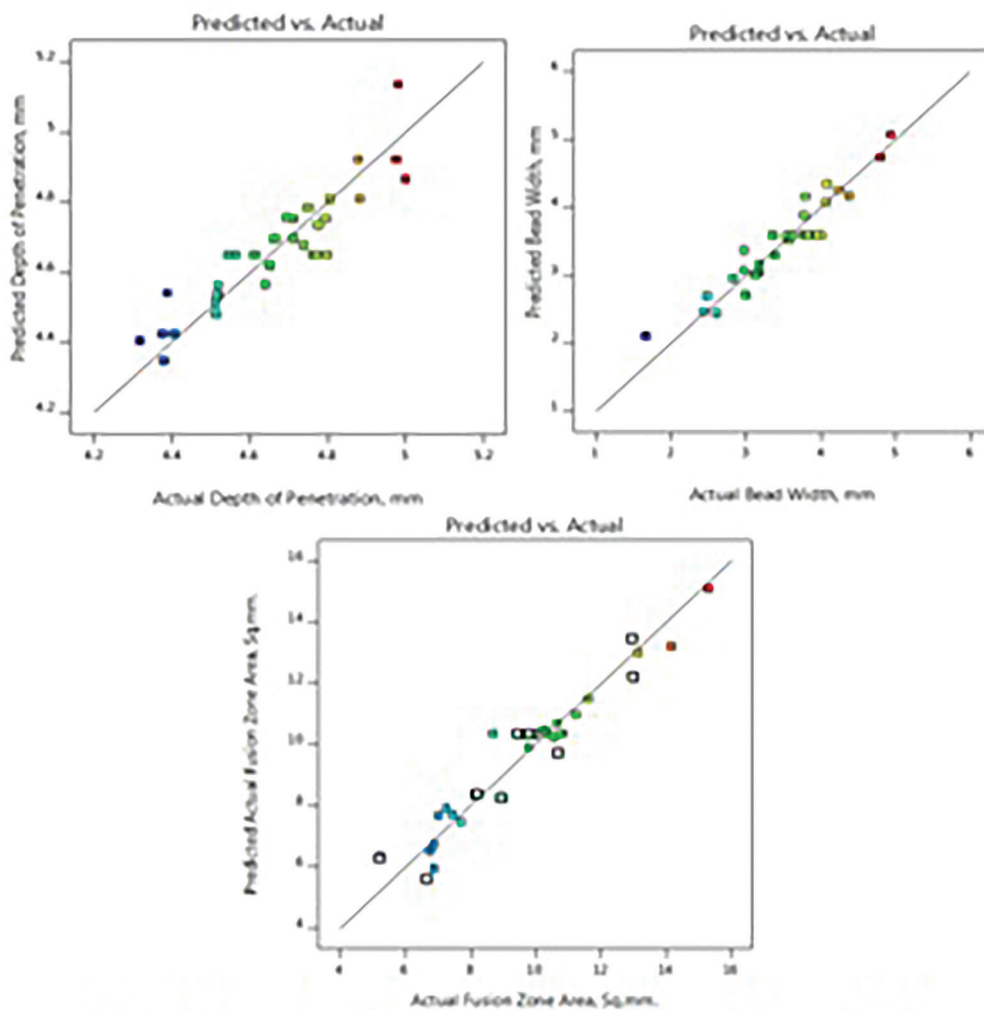


Figure 3: Scatter diagram showing (a) Depth of penetration (b) Bead width (c) Fusion Zone Area (FZ).

**Table 7:** Confirmation of the experimental results.

DESCRIPTION	DEPTH OF PENETRATION (DP)	BEAD WIDTH (BW)	FUSION ZONE AREA (FZ)
Exp. no. 1 <sup>a</sup>			
Actual	4.936	3.356	10.576
Predicted	4.8544	3.4641	10.2378
Error %	1.653	-3.221	3.197
Exp. no. 2 <sup>b</sup>			
Actual	4.985	3.659	10.210
Predicted	4.6514	3.5647	9.9498
Error %	6.692	2.577	2.548
Exp. no. 3 <sup>c</sup>			
Actual	5.00	2.712	6.659
Predicted	4.6813	2.823	7.0732
Error %	6.374	-4.092	-6.22

<sup>a</sup>Beam power: 2790 W; welding speed: 625 mm/min; focal position: -0.75; Beam Angle: 87°; Beam Offset: 0.05.

<sup>b</sup>Beam power: 3000 W; welding speed: 800 mm/min; focal position: -0.5; Beam Angle: 90°; Beam Offset: 0.1.

<sup>c</sup>Beam power: 3210 W; welding speed: 975 mm/min; focal position: -0.25; Beam Angle: 93°; Beam Offset: 0.15.

### 3.3. Effect of input parameters on output responses

The effect of input parameters on output responses is clearly explained by Figures 4(a), (b), and (c). In those, all the five input parameters, laser beam power (A), welding speed (B), focal position (C), beam angle (D) and beam offset (E) are detailed against the output responses.

#### 3.3.1. The Impact of laser beam strength

Figure 4(a) demonstrates that the increasing depth of penetration with increased laser power and an increase in welding speed results in reduced penetration. Figure 4(b) demonstrates the reduced bead width with an increased beam power. Furthermore, as shown in Figure 4(b), a wider laser beam increases bead width because the material melts over a larger surface area, whereas a concentrated beam has a smaller area to spread throughout the material, resulting in a minimal bead width [35–38]. Figure 4(c) shows a progressive increase in the weld bead area and a modest decrease in values with increased laser power. In the macrographs of each sample presented in Figure 2, these impacts may be seen. For example, sample 17 was given the least amount of power, which led to the least amount of melting and the smallest bead area.

#### 3.3.2. Welding speed influence

Figures 4(a), (b), and (c) and 8 clearly show that response values decrease with an increase in welding speed. In addition, increasing the welding speed results in less complete melting of the materials, resulting in porosity and a lower weld bead profile of sample no. 20. In the meantime, the melting rate is high and the weld profile area is higher at the lowest speed. This is an example of a sample in Figure 2. Bead area and porosity are strongly

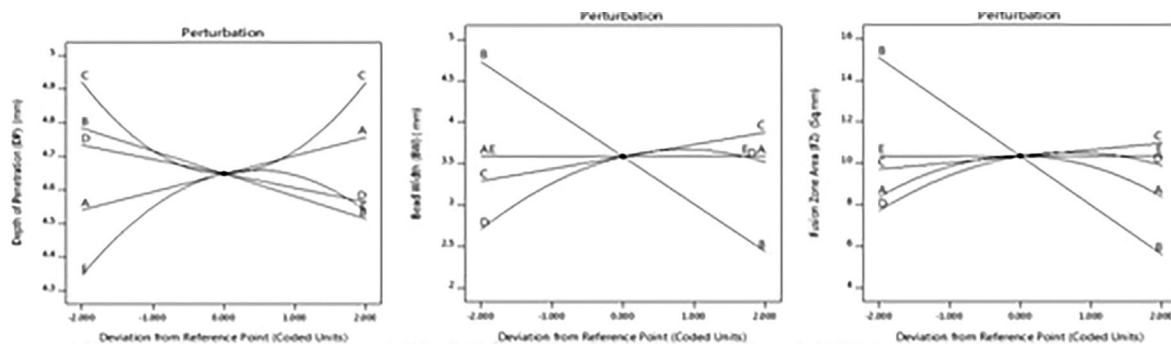


**Figure 4:** Perturbation plot (a) Depth of penetration (b) Bead width (c) Fusion zone area (FZ).

influenced by weld speed. Even though all three elements were involved, the strength of the dissimilar joint was influenced drastically by the laser power and speed [39].

### 3.3.3. The influence of focal position

Figure 4(a) shows that the penetration depth decreases up to the focus point, then increases from  $-0.5$  mm to 0 mm. This is due to the interaction between welding speed and beam angle [40], which are the key factors impacting penetration depth outlined in Figure 5(a). With focusing and defocusing focal positions, the focal position shows the increased and decreased area of the Fusion Zone (FZ), as shown in Figure 4(c). If the focal location was in the lower range, the macrograph of the bead profile in Figure 2 shows greater porosity of sample no. 21. When the range was greater, the same results were seen.

### 3.3.4. The impact of beam alignment

It is evident from Figure 4(a) that the maximum penetration depth is formed when more material melts at lower angles. Because of the wide range of differences in thermal conductivity and laser absorption, it is extremely difficult to compensate for the melting ratios of different materials [41]. An increase in welding speed results in deeper penetration at a  $93^\circ$  beam angle, as shown in Figure 5(a). With a higher rate of acceleration, the decrease in angle has the opposite effect. Figure 4(b) shows that the bead width and Fusion Zone Area do not change significantly when the beam angle is varied. As a result, the beam angle has no substantial impact on either response.

### 3.3.5. Effects of beam offset

The beam offset has an effect on the penetration angle. Figure 5(b) illustrates the influence of beam offset and beam angle on penetration depth. Beam offset and beam angle increase until their central values become stable in this scenario, and as a result, the response value rises. The melting temperature and thermal conductivity of the different materials can cause problems when a dissimilar joint is being joined together [42]. The offset distance can be tweaked to fix this problem. Response to depth of penetration increases up to the middle and then proceeds steadily towards nickel with the increase in beam offset distances. Figure 4(b) shows that the beam offset has no substantial effect on the bead width or Fusion Zone Area. Figure 4(c) also shows that the beam offset has no major impact on bead width.

## 3.4. Response plots and contour plots analyzed

The depth of penetration and welding speed both decrease as the latter increases. In Figure 6(a), (b) and Figure 7(a), (b), the depth of penetration reduces to a minimal value with a rise in focal position and then steadily increases with the subsequent increase in beam power. For example, the rate of penetration increases more rapidly at lower beam angles and focal positions, as depicted in Figure 8(b). Bead width is affected by the interplay between welding speed and focus location, as seen in Figure 9(a) and (b). As the focal position is lowered, the bead width grows, whereas as the welding speed is increased, the bead width reduces. Figure 10(a) and (b) contour plot and surface graph show that bead width increases when welding speed decreases and beam offset increases. According to Figure 11(a) and (b), the Fusion Zone Area tends

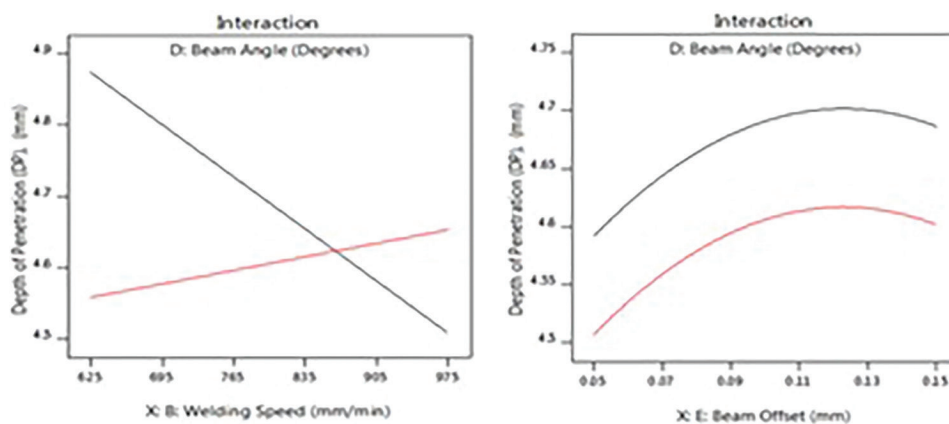


Figure 5: Interaction plot of the specimens (a) Welding speed and beam angle on depth of penetration (b) Beam-offset and beam angle on depth of penetration.

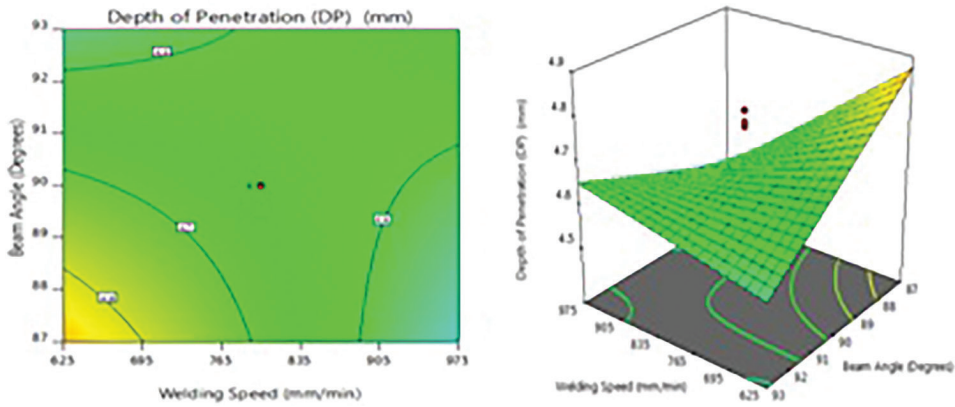


Figure 6: The interaction effects of welding specimens (a) Welding speed and beam angle on depth of penetration (b) Welding speed and beam angle on depth of penetration.

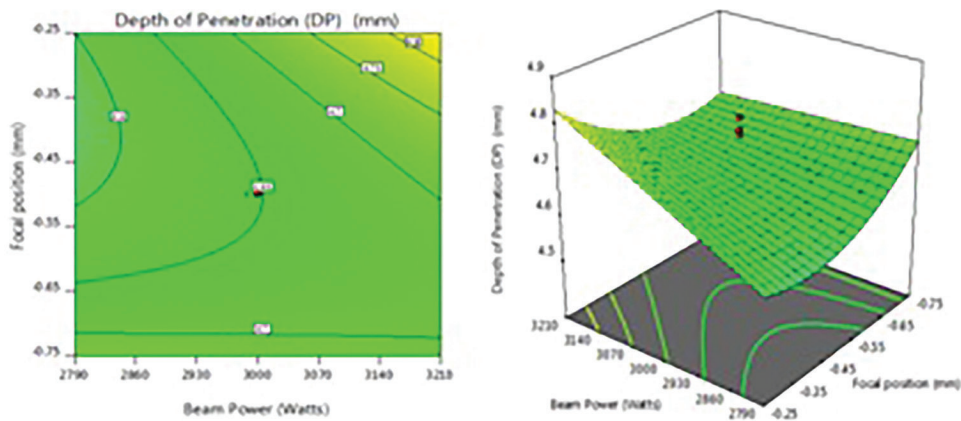


Figure 7: The interaction effects of welding specimens (a) Beam power and focal position on depth of penetration (b) Beam power and focal position on depth of penetration.

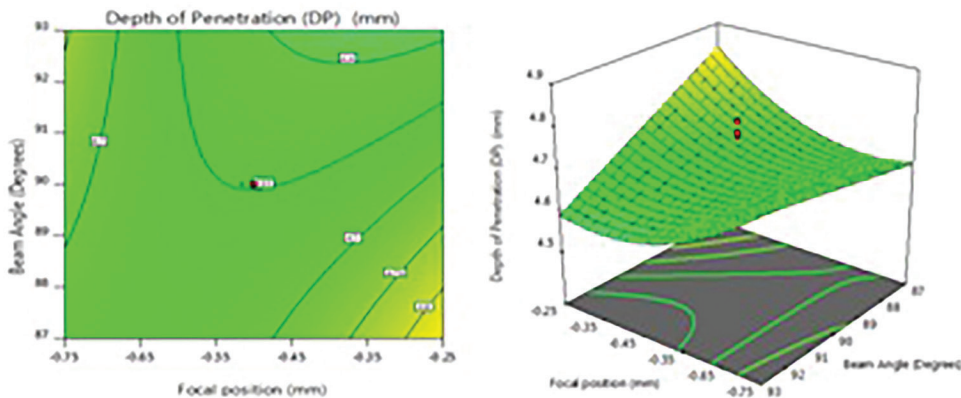


Figure 8: The interaction effects of welding specimens (a) Beam angle and focal position on depth of penetration (b) Beam angle and focal position on depth of penetration.

to rise continuously with a slow beam angle and greatly at welding speed. This suggests that welding speed has a favourable effect on weld width, as was previously mentioned in this article. Increasing the beam angle decreases weld width. For this reason, weld duration is reduced and less heat is provided as a result of increasing welding speed. Because of this, the molten material volume decreases during the melting process [43–46].

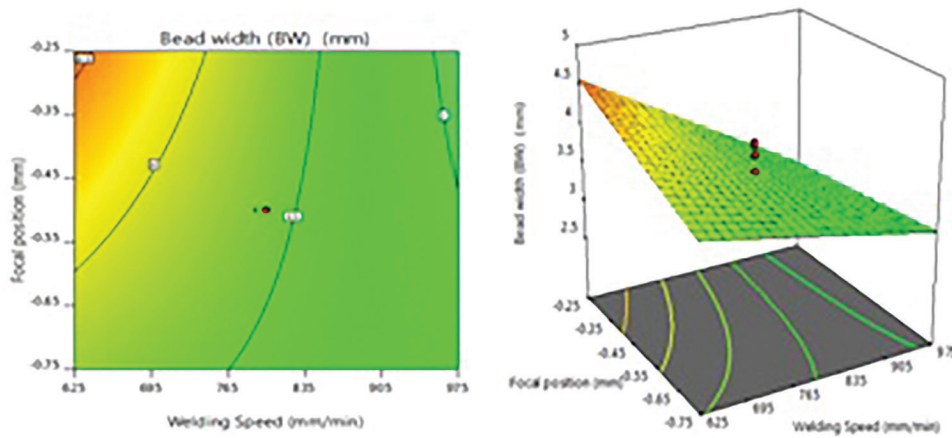


Figure 9: The interaction effects of welding specimens (a) Welding speed and focal position on bead width (b) Welding speed and focal position on bead width.

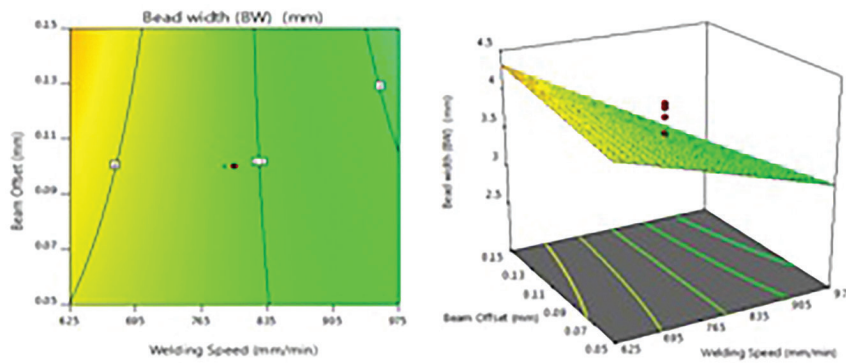


Figure 10: The interaction effects of welding specimens (a) Welding speed and beam offset on bead width (b) Welding speed and beam offset on bead width.

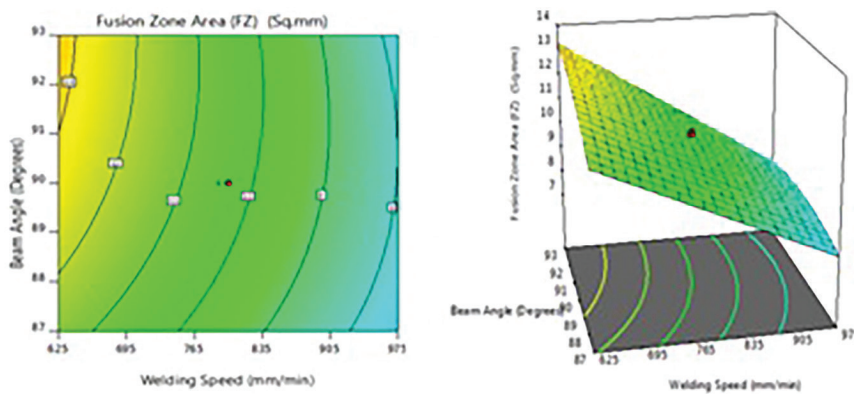


Figure 11: The interaction effects of welding specimens (a) Welding speed and beam angle on fusion zone area (fz) (b) Welding speed and beam angle on bead width.

#### 4. WORKFLOW OPTIMIZATION

Table 8 served as the basis for the optimization criteria, and each process input and output variable and reaction has its own specific purpose and weighting in the hierarchy of importance. Maximum penetration depth, minimal bead width, and Fusion Zone Area are the primary objectives in the current procedure. First, all of the process parameters were set to their working range.

**Table 8:** List of optimization criteria and their relative weight.

NAME	FIRST CRITERIA	SECOND CRITERIA	IMPORTANCE
Beam Power	is in range	Minimize	3
Welding Speed	is in range	Maximize	3
Focal position	is in range	is in range	3
Beam Angle	is in range	is in range	3
Beam Offset	is in range	is in range	3
Depth of Penetration	Maximize	Maximize	5
Bead Width	Minimize	Minimize	3
Fusion Zone Area	Minimize	Minimize	3

**Table 9:** For the first criterion of the best welding solution.

NO.	BP	WS	FP	BA	BO	DP	BW	FZ	D
1	3210.000	975.000	-0.250	87.000	0.150	4.771	2.466	6.278	0.765
2	3209.999	967.273	-0.250	87.000	0.148	4.782	2.528	6.414	0.761
3	3209.988	974.754	-0.250	87.147	0.150	4.771	2.489	6.347	0.761
4	3209.999	969.846	-0.251	87.000	0.146	4.779	2.521	6.408	0.761
5	3209.999	974.993	-0.253	87.000	0.144	4.774	2.509	6.399	0.759

**Table 10:** For the second criterion of the best welding solution.

NO.	BP	WS	FP	BA	BO	DP	BW	FZ	D
1	2790.002	975.000	-0.750	92.988	0.091	4.803	3.461	6.764	0.770
2	2791.099	974.969	-0.750	93.000	0.099	4.812	3.464	6.910	0.770
3	2790.001	974.944	-0.750	93.000	0.079	4.785	3.454	6.528	0.769
4	2792.377	974.873	-0.750	93.000	0.101	4.813	3.464	6.964	0.769
5	2790.001	974.999	-0.750	92.914	0.097	4.805	3.465	6.887	0.768

**Table 11:** Testing of bead geometry in search of optimal solutions.

DESCRIPTION	DEPTH OF PENETRATION (DP)	BEAD WIDTH (BW)	FUSION ZONE AREA (FZ)
Predicted Value	4.803	3.461	6.764
Measured Value	4.882	3.3841	6.887
Error %	1.6448	-2.2219	1.8184

Error, % = [(measured value – predicted value) / predicted value] × 100.

In the second criterion, the process parameters were aimed at being minimised while welding speed was maximised. When conducting the numerical optimization, all of the other input parameters were set in their working ranges. As a result, goals were set using the same approach as the first criteria. Aside from that, the importance of the input parameters and the output replies was kept constant for the two criteria. According to Tables 9 and 10 for first and second criteria, these are the best outcomes. When comparing the two findings on the basis of desirability value, the second criterion comes out on top. For the graphical optimization method, the same criteria can be applied. In the graphical method, the overlay plot can be used to find the best area [47, 48].

#### 4.1. Conformity tests for optimization

##### 4.1.1. Verification of bead geometry through experimentation

Table 11 depicts the results of a conformance test for the optimised input and output replies. The completed bead profile values are within the acceptable range of error percentage between the predicted and measured values. Figure 12 depicts the bead profile of the optimal conformance specimen.

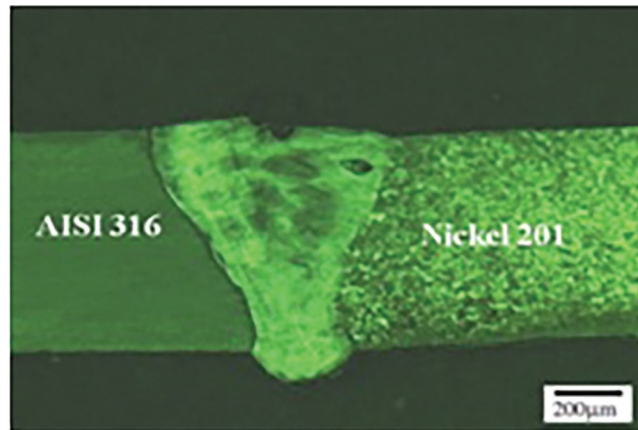


Figure 12: Profile of a bead for conformity test.

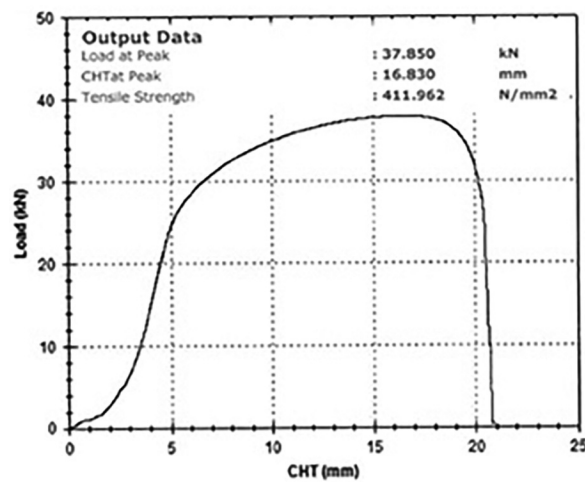


Figure 13: The optimised specimen's load vs. elongation curve.

#### 4.1.2. Results of the tensile test

The tensile test is carried out as per ASTM E 8–16 as a standard and using the Electro-Mechanical Universal Testing Machine UNITEK 9450. EDM wire cutters were used to prepare the welded samples of the tensile specimens. AISI 316 and Nickel 201 CO<sub>2</sub> laser welding were used to create a dissimilar metal junction with a tensile strength of over 412 MPa that was deemed appropriate for use. Figure 13 shows the shattered specimen after tensile testing on an optimised specimen. It appears that weld strength is comparable [49, 50] to that of nickel 201, and that the results are satisfactory. The sample's fusion is excellent, and no weld failures were discovered. There was a maximum force of 37.85 kN and a tensile stress of 411.962 N/mm<sup>2</sup> on the optimised specimen, as depicted in Figure 13.

#### 4.2. The optimized specimen's microstructure

Microstructure studies were carried out on the optimised specimen for improved bonding of nickel 201 and AISI316. Mechanical characteristics indicate that the two metals are well-suited to each other. However, the specimen's microstructure in Figure 14(a) depicts the microstructure of a gamma (nickel) solid solution with large, equiaxed grains of grain size. The annealing twins (AT) are seen in the grains.

Figure 14(b) exhibits fine austenite grains within annealing twins (AT) and less than 5% free ferrite is seen. Figure 14(c) shows fine dendrites of nickel solid solution and there is some delta ferrite in the interdendritic area. The solidification structure displays a coarse columnar structure in the sample, which indicates successful fusion in the weld joint between the dissimilar metals [51]. Because welding is a dynamic process, the orientation of the temperature isotherms changes during a weld. So, it is found that the main direction of growth of the austenite is different from that of the delta grains. The microstructure and mechanical properties of the improved process specimen significantly support the association between dissimilar welding and a good joint.

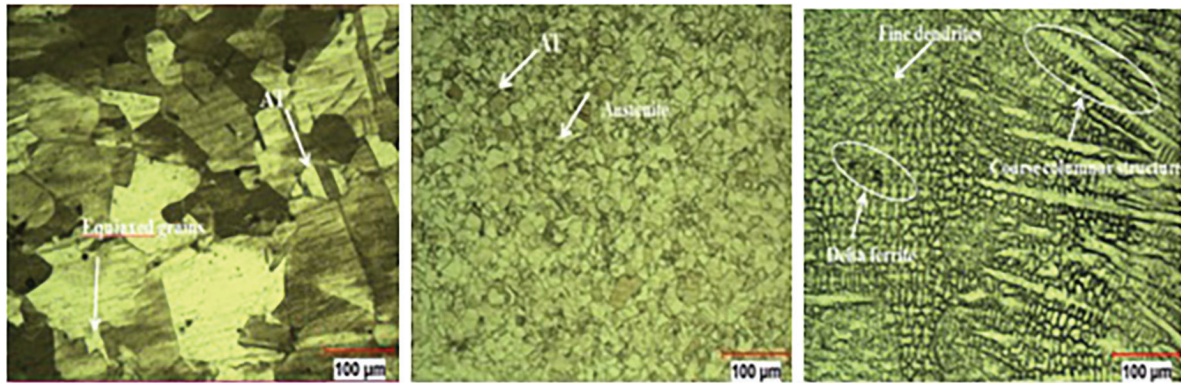


**Figure 14:** Microstructure analysis of various metals and weldments. (a) Base metal of Nickel 201 (b) Base metal of AISI 316 (c) Weld specimen.

## 5. CONCLUSIONS

The following are the findings of the above investigations:

- The best input process parameters for a high-quality dissimilar weld of AISI 316 and nickel 201 is a laser beam power of 2790 W. This is the best value for an input parameter when making dissimilar joints. The speed of the welding, which should be 975 mm/s with a focal point of -0.75 mm, is one of the most important inputs.
- The best outputs are achieved with a beam angle of 92.98° and an offset distance of 0.091 mm toward the nickel side.
- Numerical optimization is a tool for determining the link between the input parameters and the effective weld joint. However, to achieve higher weld quality, the most important factor in determining the output response is the depth of penetration, which is satisfied by the second requirement.
- The dissimilar joint of AISI 316 and nickel 201 passed all conformance tests of bead geometry, tensile test, and microstructure. The confirmation test revealed that the process parameters had been tuned to their maximum efficiency. For the optimised dissimilar joint weld bead profiles, nearly identical weld bead profiles were predicted. The computed and experimental error percentages are 1.64%, -2.22%, and 1.81%, respectively, for penetration depth, bead width, and fusion zone area.
- The tensile strength of the specimen of nickel 201 base metal is around 412 MPa. The interdendritic zone in the optimal specimen demonstrates strong fusion at the weld joint between the dissimilar metals, as shown by the microstructure measurements. The interdendritic zone also has a coarse columnar solidification structure.

Hence, the 4 kW CO<sub>2</sub> laser welding machine makes it possible to weld materials that are very different from one another. The dissimilar joints of AISI 316 and nickel 201 were the applications of aerospace and atomic power plants.

## 6. ACKNOWLEDGMENTS

The authors sincerely acknowledge for the technical support provided by Dr. K. Manonmani, Associate Professor, Government College of Technology, Coimbatore, India and Mr. K. Kanagaraj & Mr. A. Manikandan from CK Airtech, Hosur, India.

## 7. BIBLIOGRAPHY

- [1] GUPTA, P.D., “Laser applications in indian nuclear power programme”, *Energy procedia*, v. 7, pp. 560–576, 2011.
- [2] OKONKWO, B.O., MING, H., WANG, J., *et al.*, “Microstructural characterization of low alloy steel A508 – 309/308L stainless steel dissimilar weld metals”, *International Journal of Pressure Vessels and Piping*, v. 190, 104297, 2021.
- [3] ARECCHI, F.T., SCHULZ-DUBOIS, E.O., *Laser Handbook*. v. 2. New York: North-Holland, 1972.
- [4] JAFARI, D., VANEKER, T.H.J., GIBSON, I., “Wire and arc additive manufacturing: Opportunities and challenges to control the quality and accuracy of manufactured parts”, *Materials & Design*, v. 202, 109471, 2021.

- [5] KRISAM, S., BECKER, H., SILVAYEH, Z., *et al.*, “Formation of long-range ordered intermetallic  $\eta'$  phase and the involvement of silicon during welding of aluminum-steel sheets”, *Materials Characterization*, v. 187, 111862, 2022.
- [6] PALANIVEL, R., DINAHARAN, I., LAUBSCHE, R.F., “Microstructure evolution and mechanical characterization of Nd:YAG laser beam welded titanium tubes”, *Materials Characterization*, v. 134, pp. 225–235, 2017.
- [7] PARMAR, R.S., “*Welding processes and technology*”. Bangalore: Khanna Publishers, 1997.
- [8] ZHOU, S., WANG, B., WU, D., *et al.*, “Follow-up ultrasonic vibration assisted laser welding dissimilar metals for nuclear reactor pump can end sealing”, *Nuclear Materials and Energy*, v. 27, 00975, 2021.
- [9] TJONG, S.C., ZHU, S.M., HO, N.J., *et al.*, “Microstructural characteristics and creep rupture behavior of electron beam and laser welded AISI 316L stainless steel”, *Journal of Nuclear Materials*, v. 227, n. 1–2, pp. 24–31, 1995.
- [10] RAMACHANDRAN, S., LAKSHMINARAYANAN, A.K., “An insight into microstructural heterogeneities formation between weld sub regions of laser welded copper to stainless steel joints”, *Transactions of Nonferrous Metals Society of China*, v. 30, n. 3, pp. 727–745, 2020.
- [11] MIGLIORE, L.R., *Laser materials processing*. California: Laser Kinetics, 2003.
- [12] ASM Handbook., *Welding, Brazing and Soldering*. v. 6. Ohio: ASM, 1972.
- [13] CARLSON, K.W., “The role of heat input in deep penetration laser welding”, In: *4th International Congress on application of Lasers and Electro Optics*, pp. 49–57, San Francisco, 1985.
- [14] SHAIBU, V.B., SAHOO, S.K., KUMAR, A., “Computational modeling of dissimilar metal CO<sub>2</sub> laser welding: Applied to copper and 304 stainless steel”, *Procedia Engineering*, v. 127, pp. 208–214, 2015.
- [15] CHANDRASEKARAN, K., KUMAR, P.R., RAMANATHAN, R., *et al.*, “Characteristic analysis of dissimilar metal weld for AISI304 with SA213T22 in super heater coils”, *Materials Today: Proceedings*, v. 45, pp. 6788–6793, 2021.
- [16] JU, H.M., ZHUO, S., LIU, J., *et al.*, “Effects of long-term thermal aging on the microstructure and mechanical behaviors of 16MND5/Alloy 152 dissimilar metal weld”, *Journal of Materials Research and Technology*, v. 18, pp. 3961–3970, 2022.
- [17] KURYNTSEV, S.V., MORUSHKIN, A.E., GILMUTDINOV, K.H., “Fiber laser welding of austenitic steel and commercially pure copper butt joint”, *Optics and Lasers in Engineering*, v. 90, pp. 101–109, 2017.
- [18] KARTHIKEYAN, C., ANBAZHAGAN, V., MITRA, T.K., *et al.*, “Laser welding of stainless steel sheets with augmentation of gas tungsten arc”, *Welding Research Institute Journal*, v. 16, pp. 05–13, 1995.
- [19] KUMAR, V.A., VENKATESAN, E., BALDEV, R., *et al.*, “Laser welding of dissimilar metals with large thickness ratio”, *Indian Welding Journal*, v. 29, n. 2, pp. 17–23, 1996.
- [20] Anawa, E.M., Olabi, A.G., Hashmi, M.S.J., “Application of Taguchi method to optimise dissimilar laser welded components”, *Int. J. Manufacturing Technology and Management*, v. 15, pp. 219–227, 2008.
- [21] ZHOU, S., CHAI, D., YU, J., *et al.*, “Microstructure characteristic and mechanical property of pulsed laser lap-welded nickel-based superalloy and stainless steel”, *Journal of Manufacturing Processes*, v. 25, pp. 220–226, 2017.
- [22] DAWES, C., *Laser Welding*. New York: Abington Publishing, 1992.
- [23] RUGGIERO, A., TRICARICO, L., OLABI, A.G., *et al.*, “Weld-bead profile and costs optimisation of the CO<sub>2</sub> dissimilar laser welding process of low carbon steel and austenitic steel AISI316”, *Optics & Laser Technology*, v. 43, pp. 82–90, 2011.
- [24] VELMURUGAN, C., SUBRAMANIAN, R.S., THIRUGNANAM, S., *et al.*, “Experimental study on the effect of SiC and graphite particles on weight loss of Al 6061 hybrid composite materials”, *Journal of Technology and Science Education*, v. 2, pp. 49–68, 2011.
- [25] RINNE, J., SEFFER, O., NOTHDURFT, S., *et al.*, “Investigations on the weld metal composition and associated weld metal cracking in laser beam welded steel copper dissimilar joints”, *Journal of Materials Processing Tech*, v. 296, 117178, 2021.
- [26] DONG, L., MA, C., PENG, Q., *et al.*, “Microstructure and stress corrosion cracking of aSA508-309L/308L-316L dissimilar metal weld joint in primary pressurized water reactor environment”, *Journal of Materials Science & Technology*, v. 40, pp. 1–14, 2019.

- [27] KANNAN, T., MURUGAN, N., “Prediction of ferrite number of duplex stainless steel clad metals using RSM”, *Welding Journal*, v. 85, pp. 91–100, 2006.
- [28] MANONMANI, K., MURUGAN, N., BUVANASEKARAN, G., “Effects of process parameters on the bead geometry of laser beam butt welded stainless steel sheets”, *International Journal of Advanced Manufacturing Technology*, v. 32, pp. 1125–1133, 2007.
- [29] ACHERJEE, B., KUAR, A.S., MITRA, S., *et al.*, “Experimental investigation on laser transmission welding of PMMA to ABS via response surface modeling”, *Optics & Laser Technology*, v. 44, pp. 1372–1383, 2012.
- [30] TAN, C., YANG, J., ZHAO, X., *et al.*, “Influence of Ni coating on interfacial reactions and mechanical properties in laser welding-brazing of Mg/Ti butted joint”, *Journal of Alloys and Compounds*, v. 764, pp. 186–201, 2018.
- [31] LONGLONG, G., HUALIN, Z., SHAOHU, L., *et al.*, “Formation quality optimization and corrosion performance of inconel 625 weld overlay using hot wire pulsed TIG”, *Rare Metal Materials and Engineering*, v. 45, pp. 2219–2226, 2016.
- [32] MONTGOMERY, D.C., *Design and Analysis of Experiments*. 2 ed. New York: Wiley, 1984.
- [33] KHURI, A.I., CORNELL, J.A., “*Response Surfaces Design and Analysis*”. 2 ed. New York: Marcel Dekker, 1996.
- [34] LIAO, Y.C., YU, M.H., “Effects of laser beam energy and incident angle on the pulse laser welding of stainless steel thin sheet”, *Journal of Materials Processing Technology*, v. 190, pp. 102–108, 2007.
- [35] KHAN, M.M.A., ROMOLI, L., FIASCHI, M., *et al.*, “Laser beam welding of dissimilar stainless steels in a fillet joint configuration”, *Journal of Materials Processing Technology*, v. 212, pp. 856–867, 2012.
- [36] ZHANG, Y., CAI, Z., LI, X., *et al.*, “Investigation on solidification and phase transformation of heterogeneous interface structure in dissimilar metal weld between high Cr heat-resistant steel and nickel-based alloy 617”, *Journal of Manufacturing Processes*, v. 62, pp. 257–261, 2021.
- [37] LI, S., HU, L., DAI, P., *et al.*, “Influence of the groove shape on welding residual stresses in P92/SUS304 dissimilar metal butt-welded joints”, *Journal of Manufacturing Processes*, v. 66, pp. 376–386, 2021.
- [38] LI, X., CAI, Z., CHEN, X., *et al.*, “Characterization and formation mechanism of ultra-fine ferrite grains in dissimilar metal weld between austenitic stainless steel and low alloy ferritic steel”, *Materials Characterization*, v. 171, 110777, 2020.
- [39] KASMAN, S., “The effects of pin offset for FSW of dissimilar materials: A study for AA 7075 – AA 6013”, *Matéria (Rio J.)*, v. 25, n. 2, e–12612, 2020.
- [40] HAUPT, W., RIFFEL, K.C., FANEZI, C., *et al.*, “Analysis of metallurgic transformations on UNS S31803 duplex stainless steel HAZ welded by pulsed GMAW process”, *Matéria (Rio J.)*, v. 22, n. 1, e11805, 2017.
- [41] PÉREZ, H., TUFARO, L., BERARDO, L., “Hernán svoboda corrosion behavior of friction stir welds on AA7075-T651: Galvanic evaluation”, *Matéria (Rio J.)*, v. 23, n. 2, e-12053, 2018.
- [42] NADALE, H.C., SVOBODA, H.G., “Fatigue life of PAW welded joints of high strength microalloyed boron steels”, *Matéria (Rio J.)*, v. 23, n. 2, e11996, 2018.
- [43] VARMA, A., YADAVALLI, A.K., “Failure analysis of a reheater tube dissimilar metal weld failure in a 500 MW power plant”, *Engineering Failure Analysis*, v. 118, 104851, 2020.
- [44] JIANG, Z., CHEN, X., YU, K., *et al.*, “Improving fusion zone microstructure inhomogeneity in dissimilar-metal welding by laser welding with oscillation”, *Materials Letters*, v. 261, 126995, 2019. <https://doi.org/10.1016/j.matlet.2019.126995>
- [45] PARANTHAMAN, V., DHINAKARAN, V., SHREE, M.V., “Optimization of CO<sub>2</sub> welding process on dissimilar metals”, *Materials Today: Proceedings*, v. 39, pt. 1, pp., 420–423, 2021.
- [46] MADHANKUMAR, S., ASHWIN, S., ROBERT, J.A., *et al.*, “Experimental investigation on ultimate tensile strength of laser butt welded inconel 718 alloy and 2205 duplex stainless steel”, *Materials Today: Proceedings*, v. 45, pt. 7, pp. 6783–6787, 2021.
- [47] BENYOUNIS, K.Y., OLABI, A.G., HASHMI, M.S.J., “Effect of laser welding parameters on the heat input and weld-bead profile”, *Journal of Materials Processing Technology*, v. 164–165, n. 3, pp. 978–985, 2005.
- [48] LIU, D., WANG, W., ZHA, X., *et al.*, “Effects of groove on the microstructure and mechanical properties of dissimilar steel welded joints by using high-entropy filler metals”, *Journal of Materials Research and Technology*, v. 13, pp. 173–183, 2021.

- [49] RAMACHANDRA MURTHY, A., GANDHI, P., VISHNUVARDHAN, S., *et al.*, “Crack growth analysis and remaining life prediction of dissimilar metal pipe weld joint with circumferential crack under cyclic loading”, *Nuclear Engineering and Technology*, v. 52, pp. 2949–2957, 2020.
- [50] CALLEJA, A., TABERNERO, I., FERNÁNDEZ, A., *et al.*, “Improvement of strategies and parameters for multi-axis laser cladding operations”, *Optics and Lasers in Engineering*, v. 56, pp. 113–120, 2014.
- [51] STAT-EASE INC., *Design Expert Software, version 6. User's Guide, Technical Manual*. Minneapolis: Stat-Ease Inc., 2000.